ELECTROCHEMISTRY

Enhanced Li-ion diffusion improves N_2-to-NH_3 current efficiency at 100 mA cm^{-2}

Qiang Zhang[1]†, Huamin Li[1,2]†, Peiping Yu[3]†, Pengyu Liu[1]†, Ning Sun[1], Yiyan Wang[1], Chunlai Tu[1], Yiping Liu[4], Yan Wang[1], Xinyang Yue[1], Linlin Ma[5], Wen Wen[6], Jinyang Xu[7], Zhaofeng Liang[7], Jingyuan Ma[7], Fei Song[7], Zheng Liang[1], Hao Sun[1], Daishun Ling[1], Hongyan Liang[2], Feng Liu[1], Yongfeng Hu[8], Tao Cheng[3]*, Jun Li[1]*

Electrochemical lithium (Li)–mediated nitrogen (N_2) reduction could enable production of ammonia (NH_3) at ambient temperatures and pressures, offering a route to reduce carbon emissions in the chemical sector. However, NH_3 productivity is often limited by sluggish Li-ion desolvation and diffusion at the solid electrolyte interphase (SEI). Here, we present a concerted desolvation: diffusion layered SEI architecture that provides abundant Li-ion flux for efficient N_2 conversion toward NH_3 production at high current densities. The SEI comprises stacked inorganic layers with low ion-binding affinity and high ion-conductivity functionalities that increase Li-ion flux by two orders of magnitude. This design strategy achieved N_2 electroreduction in a 2 M lithium difluoro(oxalato)borate electrolyte with a Faradaic efficiency of 98% and an energy efficiency of 21% for NH_3 production at 100 milliamperes per square centimeter (mA cm^{-2}). The system sustained an 80% Faradaic efficiency over 40 hours, after which performance declined.

The electrochemical conversion of nitrogen (N_2) into ammonia using lithium metal as a mediator presents an appealing pathway for efficient ammonia synthesis (*1*–*3*). The efficacy of this method hinges on advancing selectivity to increase operational efficiency and accelerating reaction rates to reduce capital costs (*4*, *5*). These goals require electrodes that promote lithium-ion (Li^+) deposition, nitridation, and protonation through a series of sequential reaction steps (*6*, *7*).

In these reactions, the solid electrolyte interphase (SEI) film on the electrode, formed through the rapid interaction between active metallic lithium and organic electrolytes, serves as the medium for Li^+ transport (*7*–*11*). Nevertheless, Li^+ transport within the SEI is restricted, resulting in hindered lithium deposition as Li^+ ions encounter obstacles or react with their surroundings. The Li^+ diffusivity can drop to less than 10^{-21} m^2 s^{-1} within the SEI layer (*5*, *12*).

In a gas-phase electrolyzer, a thin SEI layer is spontaneously generated on a porous stainless-steel cloth (SSC), allowing N_2 reactants to diffuse only short distances to reach the active metallic Li on the SSC surface (Fig. 1A) (*9*, *13*). In this setup, Li^+ diffusion within the SEI layer emerges as the limiting factor for mass transport in the cathode, akin to what is observed in lithium-nitrogen (Li-N_2) batteries (*14*), resulting in a sharp rise in potential at high current densities (*15*). Enhancing the performance of Li-N_2 batteries involves designing SEI layers that strike a balance between facilitating Li^+ desolvation to expel anions and solvents and promoting Li^+ transport through the SEI to reach the cathode (*16*).

In contrast to the N_2 reduction in reversible Li-N_2 batteries, which yields Li_3N as a product for the subsequent charging process, the lithium-mediated N_2 reduction process forms Li_3N as an intermediate for ammonia production, accompanied by the release of Li^+ in the electrolyte. Consequently, the SEI layer is Li^+-deficient during the reaction (Fig. 1B). This reaction zone, where gaseous reactants interact with desolvated Li^+ at electron-conductive SSC/SEI interfaces, rapidly narrows toward the SEI/electrolyte boundary, particularly when using SEI layers with low ionic conductivity in N_2 electrolysis (*5*, *12*). This decline is further exacerbated at high current densities owing to sluggish Li^+ transport (*5*, *17*). A substantial portion of the SEI film lacks Li^+ because of its high desolvation energy and low ionic conductivity. As hydrogen evolution competes with N_2 reduction (*7*), the substantial area of the SSC surface exposed to the Li^+-depleted SEI promotes unwanted H_2 generation. Consequently, despite recent progress in electrode design (*18*–*21*) and electrolyte optimization (*3*, *22*–*24*), the partial current density for ammonia in continuous-flow Li-mediated N_2 reduction systems has remained restricted to 8 mA cm^{-2} (*21*, *23*).

High-pressure N_2 electrolysis in a batch system offers a strategy to enable N_2 reduction at high current densities: Liquefied gas electrolytes exhibit low viscosities, accelerating ion mobility for efficient Li plating and stripping processes (*3*, *25*–*27*). Nevertheless, operating under high-pressure conditions escalates the energy consumption of the system, and the use of a batch reactor has thus far constrained the energy efficiency (EE) of N_2 reduction to ~3.0% (*3*, *8*), which also does not directly lend itself to continuous ammonia production.

Here, we introduce a hybrid SEI design that, by decoupling the ion desolvation and transport processes, enables efficient lithium deposition at current densities exceeding 100 mA cm^{-2} for ammonia production in a continuous-flow N_2 reduction system. We exploited a hierarchical SEI that, with low ion-binding affinity and high ion-conductivity properties, assembles into a stacked structure with differentiated layers that favor ion desolvation and diffusion, conformally, over the cathode surface: Li^+ transport is enhanced within an inner layer comprising ion-conductive domains, whereas Li^+ desolvation takes place in an outer layer with low ion-binding affinities to enable sufficient Li^+ flux (Fig. 1C). As a result, the interface where gaseous reactants, ions, and electrons converge substantially increases the Li^+ flux by two orders of magnitude, enabling N_2 electrolysis for improved current-to-ammonia efficiency at 100 mA cm^{-2}.

Modeling of Li-ion flux across the SEI

We began by simulating the distribution of Li^+ ions in various electrolysis scenarios using finite-element models (figs. S1 and S2; see details in the supplementary materials) (*28*, *29*). We investigated how the catalytic efficiency for Li^+ electroreduction is influenced by changes in Li^+ flux within the SEI (Fig. 1, D and E). To do so, we introduced an intermediary surface channel with a thickness of 10 nm between the cathode and the electrolyte, characterized by a Li^+ diffusion coefficient (D_{SEI}) that is markedly different from that of the bulk electrolyte (D_0). As the ratio of D_{SEI} to D_0 increases, Li^+ flux is facilitated through this layer until the desolvated Li^+ ions diffuse and undergo conversion on the cathode surface. With increasing Li^+ diffusion within the SEI layer, the current for the electrochemical conversion of the gaseous reactant also increases accordingly (Fig. 1F and fig. S3).

Design of a desolvation:diffusion layered SEI

We sought to experimentally design and implement an advanced ion-transport system. We turned our attention to hierarchical SEIs, which

---

[1] Frontiers Science Center for Transformative Molecules, State Key Laboratory of Synergistic Chem-Bio Synthesis, School of Chemistry and Chemical Engineering, Shanghai Jiao Tong University, Shanghai, China. [2] School of Materials Science and Engineering, Tianjin University, Tianjin, China. [3] Institute of Functional Nano and Soft Materials, Jiangsu Key Laboratory for Carbon-Based Functional Materials and Devices, Joint International Research Laboratory of Carbon-Based Functional Materials and Devices, Soochow University, Suzhou, China. [4] State Key Laboratory of Metal Matrix Composites, School of Material Science and Engineering, Shanghai Jiao Tong University, Shanghai, China. [5] Instrumental Analysis Center, Shanghai Jiao Tong University, Shanghai, China. [6] Shanghai Synchrotron Radiation Facility, Shanghai Advanced Research Institute, Chinese Academy of Sciences, Shanghai, China. [7] Shanghai Advanced Research Institute, Chinese Academy of Sciences, Shanghai, China. [8] Sinopec Shanghai Research Institute of Petrochemical Technology, Shanghai, China. ***Corresponding author. Email: tcheng@suda.edu.cn (T.C.); lijun001@jtu.edu.cn (J.L.)** †These authors contributed equally to this work.

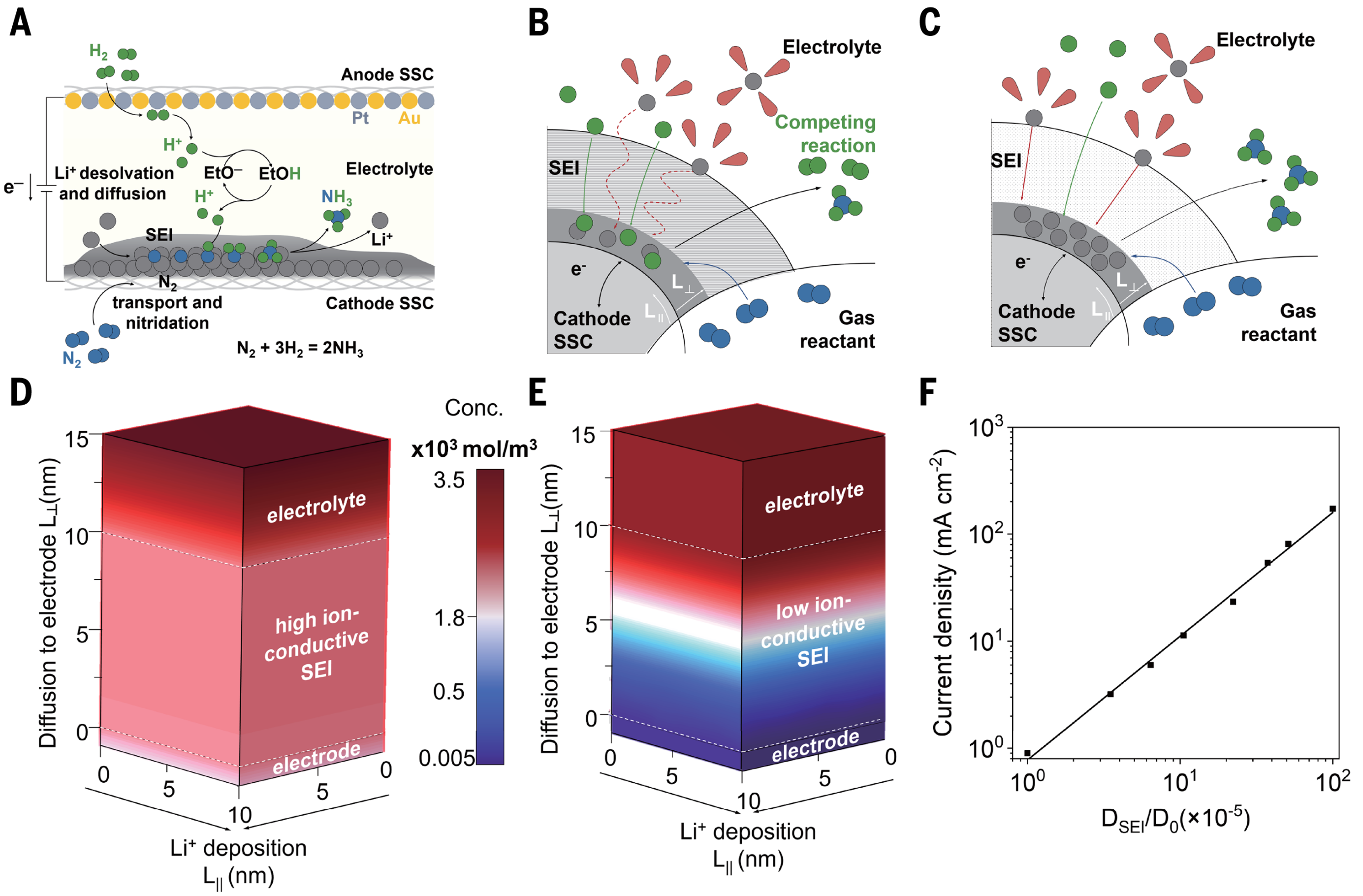

Fig. 1. Limiting current in Li-mediated nitrogen electrolysis and ion-transport SEI film. (**A**) Schematic of N_2 electrolysis in a continuous-flow electrolyzer. The metallic Li from the reduction of Li^+ on the cathode reacts with N_2 to generate lithium nitride, which is subsequently protonated with a proton source to produce ammonia. The protons are produced from hydrogen oxidation reaction on a PtAu anode catalyst (*21*) and shuttled by EtO^-/EtOH, where EtOH is ethanol. (**B** and **C**) Schematic illustrations of N_2 electrolysis at the SEI with low and high ionic conductivity. The volume in which metallic Li, N_2, and protons coexist determines the maximum available current for N_2 electrolysis. The SEI region proximate to the SSC substrate with a limited concentration of desolvated Li^+ due to sluggish ion transport promotes side reactions such as hydrogen evolution (B). When a SEI with promoted ion conductivity is formed, a substantial increase in Li^+ concentration would ensure sufficient metallic Li to react with N_2 so that all electrons participate in the desired ammonia production (C). $L_{||}$, distance parallel to the SSC surface; $L_{\perp}$, distance perpendicular to the SSC surface. (**D** and **E**) Modeled Li^+ concentration along the cathode surface for high (D) and low (E) ion-conductive SEI films, assuming different Li^+ diffusivities of D_{SEI}/D_0 valued at 10^{-3} and 10^{-5}, respectively. (**F**) Enhanced by D_{SEI}/D_0 manipulation, the modeled maximum available current density facilitates entry into the ≥100–mA cm^{-2} regime for lithium deposition. See materials and methods for details on the Li^+ transport simulations.

combine low ion-binding affinity and high ion-conductivity functionalities for Li^+ transport. Our hypothesis focused on the deliberate arrangement of these SEIs into separate desolvation and diffusion layered domains, which creates specialized pathways where a layer with low ion-binding affinity promotes ion desolvation, whereas Li^+ transport is accelerated by the ion-conductive zones (Fig. 2A).

Lithium salts such as lithium difluoro(oxalato)borate (LiDFOB), a commonly used salt in high-performance Li-ion batteries as an electrolyte (*30*, *31*), contain fluoro and oxalate groups that can be transformed into LiF and Li_2CO_3 components (fig. S4) that possess low ion-binding affinity and high ion-conductivity properties, respectively (*28*, *32*–*35*). When dissolved in a polar solvent such as tetrahydrofuran (THF), LiDFOB generates solvated Li^+ ions that interact with $DFOB^-$ anions and THF molecules (fig. S5). During electrolysis, as this solvated LiDFOB is adsorbed onto the cathode surface, we anticipated that an SEI configuration exposing the LiF-rich layer to the electrolyte would facilitate Li^+ desolvation, creating continuous percolating pathways for desolvated Li^+ ions through the Li_2CO_3-rich regions (Fig. 2B).

Characterization of the layered SEI

Seeking to promote the growth of stacked Li_2CO_3 and LiF layers toward the cathode and electrolyte surface, we prepared LiDFOB solutions in polar THF solvent. The salts were initially transformed to form a SEI layer deposited on a porous SSC substrate during continuous-flow N_2 electrolysis. Scanning electron microscopy (SEM) images revealed a homogeneous, conformal coating of nanosheets across the entire SSC (Fig. 2, C and D). Cryo–transmission electron microscopy (TEM) images, combined with detailed lattice analysis and selected area electron diffraction, unveiled the presence of a 10- to 20-nm continuous and conformal inorganic layer. This layer is composed of LiF at the outermost layer [2.00 Å, LiF(200)] (*36*), Li_2CO_3 at the intermediate layer [2.85 Å, Li_2CO_3(002)] (*37*), and Li_3N at the innermost layer [3.13 Å, Li_3N(002)] (*38*), establishing a desolvation:diffusion layered architecture (DDLA) (Fig. 2, E and F, and fig. S6).

To characterize the DDLA structural configuration, we carried out grazing-incidence synchrotron x-ray diffraction (XRD) measurements on LiDFOB-derived cathode samples (Fig. 2G and fig. S7). Both the

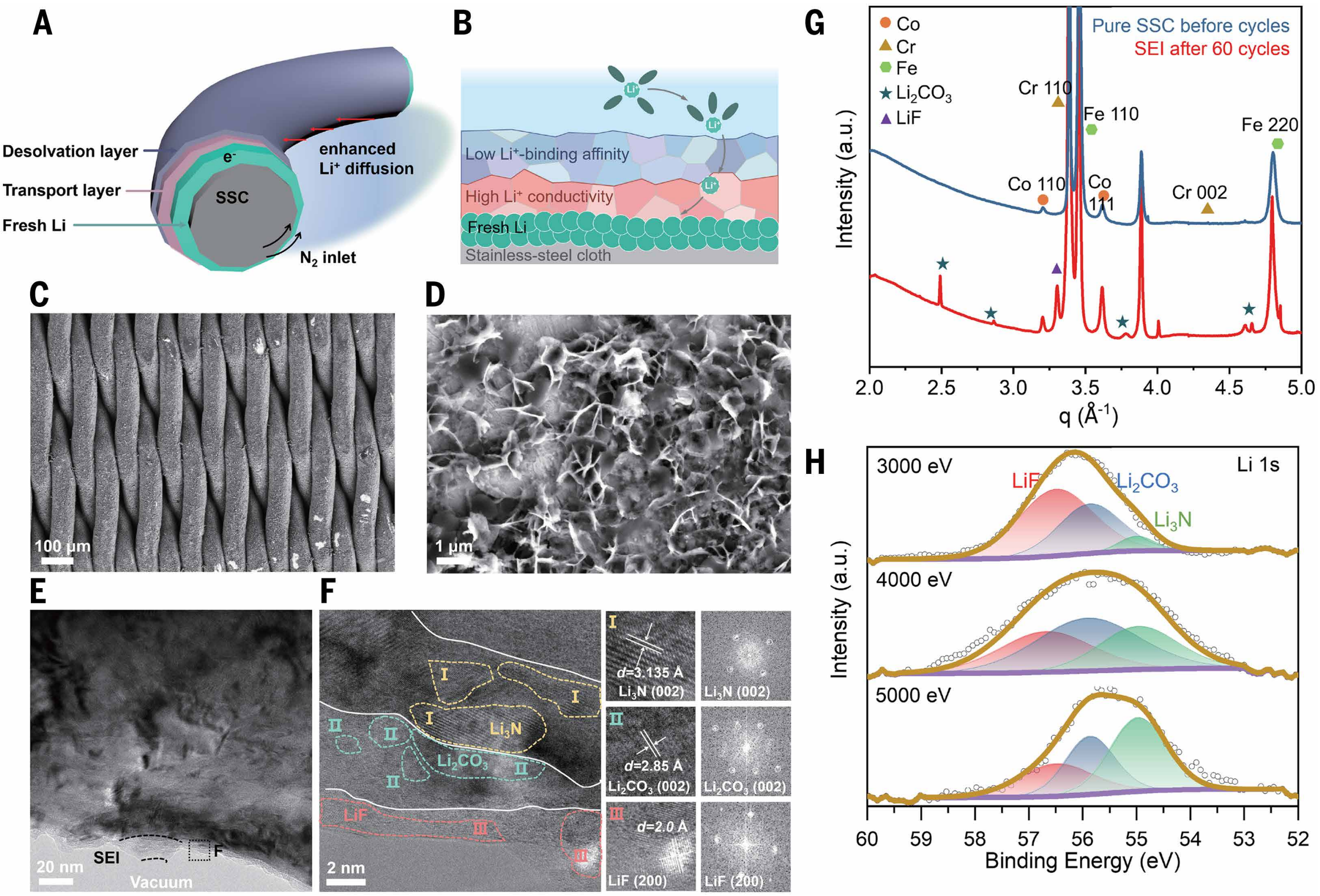

Fig. 2. Concerted desolvation:diffusion layered architecture. (**A**) Schematic of an ion-conductive SEI coated onto a SSC support. (**B**) The LiDFOB-derived SEI exhibits differentiated low ion-binding affinity and high ion-conductivity characteristics endowed by LiF and Li_2CO_3 species, respectively. (**C** and **D**) SEM images at different magnifications of the LiDFOB-derived SEI coated on the SSC surface after the 120th operating cycle at a current density of –100 mA cm^{-2}. (**E** and **F**) Cryo-TEM images at different magnifications of the LiDFOB-derived SEI, revealing a multilayer stacked structure. (**G**) Grazing-incidence synchrotron XRD spectra with an incident angle of 0.1°, showing the formation of LiF and Li_2CO_3 in the LiDFOB-derived SEI. a.u., arbitrary units; q, momentum transfer vector. (**H**) XPS depth profiles of Li 1s for the LiDFOB-derived SEI film at different incident x-ray energies. The peak-fitting procedure was performed using CasaXPS software. A Shirley background was subtracted, and the peaks were fitted with a mixing ratio of 30% Lorentzian and 70% Gaussian [GL(30)]. The goodness of the fit was assessed by the residual standard deviation, which was maintained close to 0.09 for all fits.

reference and DDLA samples exhibited similar diffraction patterns due to the SSC backbone support. The DDLA samples, in addition, revealed weak scattering at 3.3 and 2.5 $Å^{-1}$ due to the LiF and Li_2CO_3 species, respectively.

Seeking to characterize the DDLA electronic structure and verify the layered SEI configuration, we conducted depth-profiling using synchrotron-based x-ray photoelectron spectroscopy (XPS) by varying the incident x-ray energy (Fig. 2H). The Li 1s XPS spectra of the LiDFOB-derived SEI exhibited three characteristic peaks at 56.5 eV (characteristic of LiF) (*39*), 55.6 eV (associated with Li_2CO_3) (*40*), and 55.0 eV (attributed to Li_3N) (*41*). The DDLA surface showed a LiF-rich structure. Increasing x-ray energy showed that surface LiF transitioned to Li_2CO_3 and then to Li_3N at greater depths. These findings suggest that the LiF component tends to face the electrolyte, whereas Li_2CO_3 is sandwiched between LiF and Li_3N to avoid its reaction with electrolyte and metallic Li (vide infra), forming a stable SEI, consistent with the results from the C 1s, F 1s, and N 1s XPS and the time-of-flight secondary ion mass spectrometry (figs. S8 and S9).

To assess the impact of the inorganic structures on Li^+ availability, we evaluated the electrochemical performance of the SEI derived from different lithium salts. We built SEI structures consisting of different inorganic components coated over SSC substrates in a 2 M electrolyte containing either LiDFOB or lithium tetrafluoroborate ($LiBF_4$). Based on prior studies (*21*, *23*), $LiBF_4$ is reduced into a LiF-rich SEI (figs. S10 to S15). The lack of the $-C_2O_4-$ group in $LiBF_4$ can lead to a Li_2CO_3-free SEI, providing a means to assess the influence of Li_2CO_3 as an ion-conductive component on the availability of Li^+ ions. We conducted cyclic voltammetry experiments at different scan rates and calculated the Li^+ diffusion coefficients of different SEIs derived from LiDFOB and $LiBF_4$ (fig. S16). We found that the LiDFOB-derived SEI showed a considerably larger Li^+ diffusion coefficient of 5.75×10^{-13} m^2 s^{-1}, which is two orders of magnitude higher than the $LiBF_4$-derived SEI (1.63×10^{-15} m^2 s^{-1}). This result supports the notion that the enhanced Li^+ transport performance of the DDLA electrodes stems from the Li_2CO_3-rich layer, likely owing to its lower energy barrier for ion transport.

Theoretical calculations

We then sought to calculate, using density functional theory (DFT), the energy barriers for ion desolvation and diffusion. The initial Li^+ ion solvation structure was obtained through classical molecular

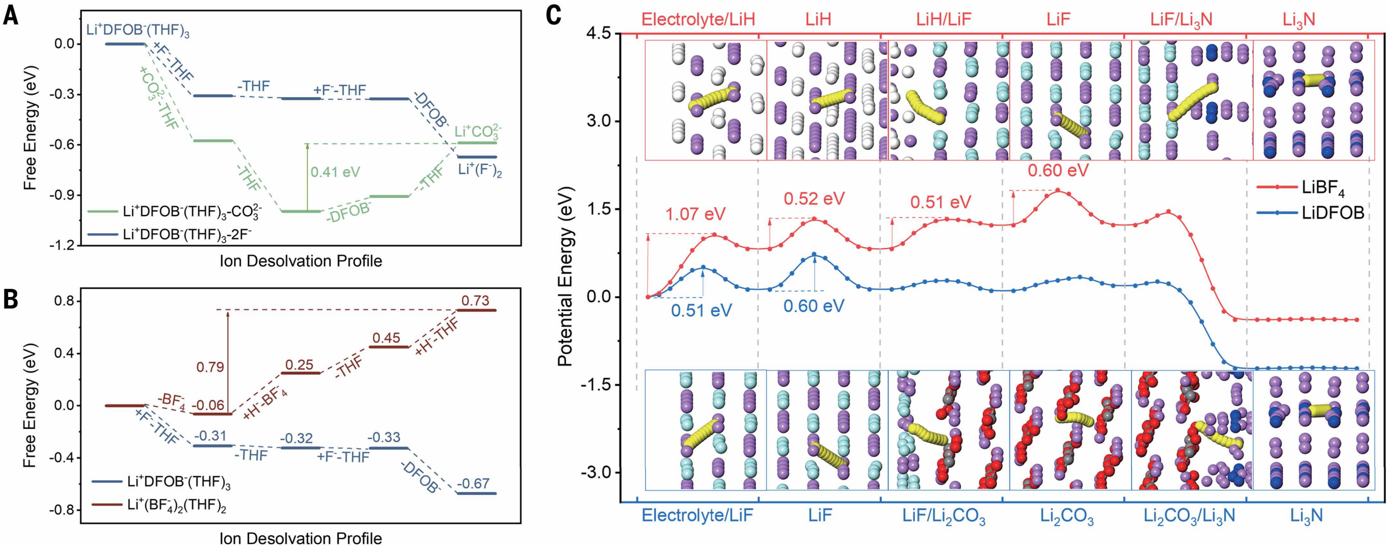

Fig. 3. DFT calculations. (**A** and **B**) Optimal Li^+ desolvation path and desolvation free energy in the LiDFOB-derived (A) and $LiBF_4$-derived (B) SEI films. (**C**) Comparison of Li^+ migration energy barriers in SEI films formed from $LiBF_4$ (top) and LiDFOB (bottom). Numerical values indicate the energy barrier at specific locations; only values exceeding 0.25 eV are displayed. The atom color scheme is as follows: white, H; magenta, Li; cyan, F; blue, N; gray, C; and red, O. The migrating Li^+ ion is shown in yellow.

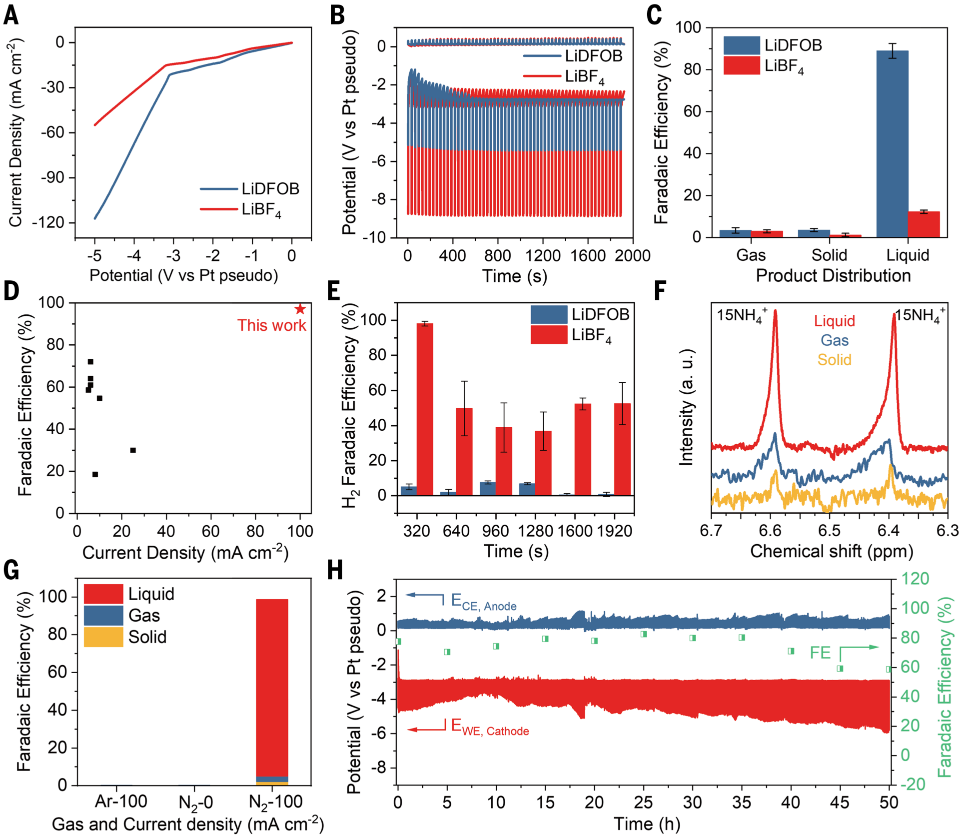

Fig. 4. Electrochemical performance of Li-mediated ammonia synthesis from N_2 reduction at 100 mA cm^{-2}. (**A**) Linear sweep voltammetry profiles of N_2 electrolysis with a scan rate of 10 mV s^{-1}. (**B**) Chronopotentiometry profiles of 50-μm SSC at a current density of −100 mA cm^{-2}. (**C**) Ammonia FE with distribution of produced ammonia in the electrolyte, electrode deposits, and gas phase-trapped acid solution. (**D**) Comparison of current density and FE for ammonia in continuous-flow N_2 electrolysis systems (table S5). (**E**) Comparison of FE_{H2} at −100 mA cm^{-2}. (**F**) Representative nuclear magnetic resonance data from $^{15}N_2$ isotope labeling experiments. ppm, parts per million. (**G**) Ammonia FEs under altering cathodic gas inputs and current conditions. (**H**) Extended ammonia electrosynthesis with controlled potential cycling at −100 mA cm^{-2} using LiDFOB. The working electrode is the 50-μm SSC. The electrolyte is 2 M LiDFOB in THF with 0.25 vol % ethanol. The potential cycling condition setting is 2 s for Li deposition at a current density of −100 mA cm^{-2} and 30 s for resting at 0 mA cm^{-2}. The error bars represent the standard deviation from at least three independent measurements.

dynamics (fig. S17 and table S1). We constructed different SEI models for the LiDFOB ($LiF/Li_2CO_3/Li_3N$) and $LiBF_4$ ($LiH/LiF/Li_3N$) systems, strictly mimicking the experimental observations (figs. S18 to S26). The LiDFOB-derived SEI showed desolvation energies of −0.67 eV for the surface LiF layer and −0.59 eV for the subsurface Li_2CO_3 layer, in which the ion desolvation in the first layer is energetically favorable but must overcome a thermodynamic limit of 0.41 eV in the second layer (Fig. 3A and fig. S18). Conversely, the $LiBF_4$-derived SEI exhibited a large desolvation energy of 0.73 eV in the surface LiH layer that must overcome a thermodynamic limit of 0.79 eV (Fig. 3B, fig. S21, and table S2). We additionally tested explicit microsolvation and constant-potential ab initio molecular dynamics, which produced the same desolvation-energy trends (figs. S23C and S24 and table S2).

We further calculated the Li^+ migration energy barriers, defect formation energy, and concentration within different SEIs based on a vacancy diffusion mechanism (Fig. 3C and fig. S27). For this, we built SEI models comprising crystalline LiF, Li_2CO_3, and Li_3N based on experimental TEM and XRD results (Fig. 2, E to G), although we acknowledge the potential influence of disordered phases and grain boundaries in modulating SEI properties. We found that the LiDFOB-derived SEI showed overall lower Li^+ migration energy barriers compared with the $LiBF_4$-derived SEI: The rate-determining step for Li^+ migration in the $LiBF_4$ system involved the movement of Li^+ from the LiH surface inward, requiring an energy barrier of 1.07 eV; by contrast, the LiDFOB system only needed to overcome an energy barrier of 0.60 eV for the rate-determining step concerning Li^+ migration within the bulk LiF. The LiF/Li_2CO_3/Li_3N SEI derived from LiDFOB electrolyte exhibits an ionic conductivity ranging from 1.57×10^{-14} to 2.19×10^{-5} S m^{-1}, which is up to several orders of magnitude greater than that of the LiH/LiF/Li_3N SEI (2.76×10^{-22} to 2.19×10^{-5} S m^{-1}) formed in $LiBF_4$ electrolyte (tables S3 and S4).

Noting that Li_2CO_3 is not stable and tends to react with metallic Li species, we postulated that the formation of Li_3N in SEI could serve as an interlayer to stabilize Li_2CO_3. To test this hypothesis, we constructed three layered models of Li_2CO_3/Li, Li_2CO_3/Li_3N/Li, and LiF/Li_2CO_3/Li_3N/Li (fig. S28). Using ab initio molecular dynamics simulation, we predicted the decomposition of Li_2CO_3 by Li metal to form Li_2O. However, this reaction was well suppressed with the addition of Li_3N and Li_3N/LiF, as confirmed by the calculated reaction free energies and energy barriers at the three interfaces (fig. S29).

To probe the dynamic evolution of SEI during electrolysis, we conducted reactive molecular dynamics simulations by applying an external voltage to the metallic Li layer (figs. S30 to S35). In both LiDFOB- and $LiBF_4$-derived SEIs, charge-state analysis within the Li_3N layer revealed reversible Li^+ reduction and metallic Li oxidation during the deposition and resting cycles (vide infra), indicating dynamic stability of both SEI structures.

Collectively, these findings indicate a full mechanistic picture for the Li-mediated N_2 electrolysis in the LiDFOB system. In a hierarchical SEI, LiF triggers Li^+ desolvation, whereas Li_2CO_3 accelerates Li^+ diffusion, enabling abundant Li^+ flux at the cathode surface and promising N_2 electrolysis at high rates.

Investigation of the Li-mediated N_2 electrolysis

Next, we focused on studying the performance of DDLA electrodes for N_2 electrolysis for ammonia production. We used a flow cell with THF electrolyte (various Li salts, 0.25 vol % ethanol proton shuttle). N_2 and H_2 flowed through the cathode (bare SSC) and anode (PtAu/SSC) compartments, respectively, with a Pt reference electrode (figs. S36 to S38). We first monitored the reduction current for different electrodes using a 2 M electrolyte (Fig. 4A). The $LiBF_4$-derived electrode showed a current density limited to less than 60 mA cm^{-2}. However, the DDLA electrode exhibited a considerably higher current density that approached 120 mA cm^{-2} under the same conditions.

We then evaluated the N_2 electrolysis performance at varying current densities ranging from 6 to 50 mA cm^{-2} (fig. S39), in which we applied a current cycling strategy—alternating between applied potential and open-circuit voltage—to enhance ammonia production, in accordance with previous reports (*21*). Ion chromatography was used to quantify the ammonia concentration (figs. S40 and S41). The $LiBF_4$-derived electrode showed an optimal Faradaic efficiency (FE) of 60% and an EE of 17.9% for ammonia at 6 mA cm^{-2}, a result that is akin to previous reports (*20*, *21*), suggesting reliability in our measurement setup. The DDLA electrode, however, reached 99% FE and 36.4% EE for ammonia at 6 mA cm^{-2}. We observed distinct ammonia FE distributions across gas, liquid, and solid phases between the two electrodes. The DDLA electrode showed predominant liquid-phase ammonia production, which we attributed to LiDFOB's chemical affinity for ammonia (fig. S42). The enhancements in FE and EE can be explained by the lower activation energies of ion desolvation and diffusion for the LiDFOB-derived SEI compared with the $LiBF_4$-derived counterpart, consistent with our DFT analysis.

The impact of Li^+ availability on performance was more acute at a higher current density of 100 mA cm^{-2} (Fig. 4, B and C). By applying a gas pressure gradient of 1.5 kPa and implementing a current cycling protocol (2-s deposition and 30-s resting; figs. S43 to S45), the DDLA electrode achieved a high ammonia FE of 98% at a full-cell voltage of −5.5 V, translating to an EE of 21% for ammonia in a 2 M LiDFOB electrolyte. This performance outcompetes literature benchmark continuous-flow Li-mediated N_2 electrolysis systems (Fig. 4D and table S5). Under similar testing conditions, the $LiBF_4$-derived electrode showed a low ammonia FE of ~16% at a markedly increased cell potential of −9.3 V (Fig. 4C), resulting in a low ammonia EE of 1.8%. Concurrently, we observed a vast production of H_2 in the $LiBF_4$ system, which, however, was well suppressed in the LiDFOB system (Fig. 4E). The observed enhancement can be explained as being due to 100× increased Li^+ flux in the LiDFOB system compared with the $LiBF_4$ system, highlighting the crucial role of the SEI structure in facilitating Li^+ diffusion and enabling efficient ammonia synthesis (figs. S46 and S47).

The effect of porosity of the SEI on N_2 transport is negligible, as both electrolyte systems form SEI films with highly porous microstructures and similar pore size distributions (fig. S48). The two different SEI layers demonstrate comparable wetting properties (fig. S49), indicating that electrode surface wettability does not markedly influence ion mobility. Electrochemical surface area measurements of SEIs formed from different electrolytes, and in systems with or without flow channels, reveal comparable values (figs. S50 and S51). This indicates that the catalytic behavior is predominantly governed by the SEI's structure and composition rather than by its electrochemical surface area.

Proton (H^+) transport in the SEI and electrolyte proton concentration critically influence ammonia generation. First, simulations revealed a lower H^+ diffusion barrier in LiDFOB-derived SEI than in $LiBF_4$-derived SEI (fig. S52), which explains why $LiBF_4$ promotes LiH accumulation and H_2 evolution (consistent with experiments in Fig. 4E and figs. S11 to S15). In LiDFOB-derived SEI, H^+ migration (1.21 eV; fig. S52) is hindered compared with Li^+ migration (0.60 eV; Fig. 3C), favoring Li^+ reduction to metallic Li. This Li reacts with N_2 to form Li_3N, which then combines with H^+ to produce ammonia while regenerating $Li^{+,}$ which aligns with the observed high ammonia FE and suppressed H_2 evolution (Fig. 4, C and E). Second, proton concentration effects were probed by varying ethanol content (0 to 0.45 vol %; figs. S53 and S54). A volcano-shaped ammonia FE trend emerged, peaking near 0.25 vol % ethanol (near-unity FE). Insufficient protons reduced both ammonia and H_2 (likely due to Li accumulation), whereas excess protons favored H_2. These results highlight the delicate balance between proton supply and transport in optimizing ammonia electrosynthesis.

We further developed a reaction-diffusion microkinetic model by extending the two earlier frameworks (*7*, *21*) to examine how enhanced Li^+ diffusion within the SEI affects product selectivity (see details in the supplementary materials). By explicitly accounting for Li^+-mediated electron flux, the model successfully reproduced FEs for both ammonia and H_2 (fig. S55 and table S6) while validating that accelerated Li^+ diffusion promotes ammonia formation.

We performed $^{15}N_2$ isotope–labeling experiments at 100 mA cm^{-2} and confirmed that the produced ammonia was indeed derived from N_2 (Fig. 4F and figs. S56 and S57) (*1*). This control was further corroborated by replacing the nitrogen with argon as a feedstock, resulting in a sharp drop in the ammonia FE from 98 to 0% (Fig. 4G). Notably, the DDLA electrode still showed a high ammonia FE of 71% from N_2 reduction at an increased current density of 150 mA cm^{-2} (fig. S58).

In a stability test of the DDLA electrode (Fig. 4H) at 100 mA cm^{-2}, the average anode and cathode potentials were less than 1 and 5.5 V, respectively, over the course of 50-hour electrolysis. Accordingly, we achieved an average ammonia FE of 80% during the first 40 hours. However, at 50 hours, the ammonia FE dropped to 60%. A single-pass electrolyte flow was used throughout the experiment to mitigate potential ammonia oxidation. The decreases in the cathode potential and FE are likely linked to an increased SEI thickness, a result that we attributed to a gradual accumulation of dead lithium on the cathode (*5*, *42*). Here, dead lithium refers to the electrochemically inactive metallic Li that fails to react with N_2.

To verify this, we sought to accelerate dead-lithium formation using a 200–mA cm^{-2} current density in LiDFOB electrolyte. Chronopotentiometry revealed stable operation for 50 cycles, followed by a gradual overpotential increase until cycle 190, and then a sharp rise to the –10 V cutoff (fig. S59A). Mirroring this trend, NH_3 FE decreased from 48.5 to 21.2% (fig. S59B). SEM and TEM images (figs. S60 and S61) showed progressive SEI thickening along with substantial metallic Li formation. XPS depth-profile analysis (figs. S62 and S63), coupled with additional reactive molecular dynamics simulations with increased deposition potentials (figs. S64 and S65), revealed distinct SEI structure evolution, in which Li_2CO_3 migrated inward while Li_3N content decreased, accompanied by metallic Li accumulation upon prolonged cycling. This redistribution destabilized the SEI as Li_2CO_3 reacted with Li metal, impeding Li^+ transport and diminishing ammonia efficiency.

Conclusions

Overall, this work presents a strategy to enable concerted Li^+ desolvation and diffusion on a SEI that partially overcomes the Li^+ transport restrictions presented in prior studies. Voltage breakdown analysis (figs. S66 and S67) indicates that improving system efficiency and long-term performance requires overcoming two key challenges: the high cathodic overpotential governing Li^+ transport and substantial voltage losses from electrolyte resistance.

REFERENCES AND NOTES

1. S. Z. Andersen *et al.*, *Nature* **570**, 504–508 (2019).
2. G. Soloveichik, *Nat. Catal.* **2**, 377–380 (2019).
3. N. Lazouski, Z. J. Schiffer, K. Williams, K. Manthiram, *Joule* **3**, 1127–1139 (2019).
4. B. H. R. Suryanto *et al.*, *Science* **372**, 1187–1191 (2021).
5. S. Li *et al.*, *Joule* **6**, 2083–2101 (2022).
6. S. Maheshwari, M. J. Janik, *Joule* **3**, 915–916 (2019).
7. S. Z. Andersen *et al.*, *Energy Environ. Sci.* **13**, 4291–4300 (2020).
8. H.-L. Du *et al.*, *Nature* **609**, 722–727 (2022).
9. K. Steinberg *et al.*, *Nat. Energy* **8**, 138–148 (2023).
10. H. Jiang, G.-F. Chen, O. Savateev, H. Wang, *Joule* **7**, 253–256 (2023).
11. K. Li *et al.*, *Science* **374**, 1593–1597 (2021).
12. S. Tu *et al.*, *Nat. Energy* **8**, 1365–1374 (2023).
13. S. J. Blair *et al.*, *Energy Environ. Sci.* **16**, 3391–3406 (2023).
14. F. Meng, X. Xiong, S. He, Y. Liu, R. Hu, *Adv. Energy Mater.* **13**, 2300269 (2023).
15. J.-Y. Li *et al.*, *Angew. Chem. Int. Ed.* **63**, e202319211 (2024).
16. Z. Zhang *et al.*, *Angew. Chem. Int. Ed.* **58**, 17782–17787 (2019).
17. X. Cai *et al.*, *J. Am. Chem. Soc.* **145**, 25716–25725 (2023).
18. K. Li *et al.*, *ACS Energy Lett.* **7**, 36–41 (2022).
19. L.-F. Gao *et al.*, *Angew. Chem. Int. Ed.* **60**, 5257–5261 (2021).
20. N. Lazouski, M. Chung, K. Williams, M. L. Gala, K. Manthiram, *Nat. Catal.* **3**, 463–469 (2020).
21. X. Fu *et al.*, *Science* **379**, 707–712 (2023).
22. M. Spry *et al.*, *ACS Energy Lett.* **8**, 1230–1235 (2023).
23. S. Li *et al.*, *Nature* **629**, 92–97 (2024).
24. X. Fu *et al.*, *ACS Energy Lett.* **9**, 3790–3795 (2024).
25. A. Tsuneto, A. Kudo, T. Sakata, *J. Electroanal. Chem.* **367**, 183–188 (1994).
26. A. Tsuneto, A. Kudo, T. Sakata, *Chem. Lett.* **22**, 851–854 (1993).
27. C. S. Rustomji *et al.*, *Science* **356**, eaal4263 (2017).
28. S. Zhang *et al.*, *Nat. Commun.* **13**, 5431 (2022).
29. L. Pang *et al.*, *ACS Energy Lett.* **9**, 3746–3753 (2024).
30. M. Li *et al.*, *J. Am. Chem. Soc.* **145**, 25632–25642 (2023).
31. M. Mao *et al.*, *Nat. Commun.* **14**, 1082 (2023).
32. J. A. Weeks *et al.*, *Adv. Mater.* **36**, e2305645 (2024).
33. J. Chen *et al.*, *Nat. Energy* **5**, 386–397 (2020).
34. K.-i. Chung *et al.*, *Microchem. J.* **75**, 71–77 (2003).
35. Q. Zhang *et al.*, *Nano Lett.* **16**, 2011–2016 (2016).
36. A. C. Thenuwara *et al.*, *ACS Energy Lett.* **5**, 2411–2420 (2020).
37. B. Han *et al.*, *Adv. Mater.* **33**, e2100404 (2021).
38. W. Cao *et al.*, *J. Energy Chem.* **76**, 648–656 (2023).
39. Z. Li *et al.*, *Nat. Commun.* **14**, 482 (2023).
40. D. Wu *et al.*, *Adv. Energy Mater.* **12**, 2200337 (2022).
41. M. S. Kim *et al.*, *ACS Nano* **17**, 3168–3180 (2023).
42. W. Zhang *et al.*, *Nature* **626**, 306–312 (2024).
43. Q. Zhang, H. Li, P. Yu, T. Cheng, J. Li, Enhanced Li-ion diffusion improves N_2-to-NH_3 current efficiency at 100 mA cm^{-2}. Figshare (2025); https://doi.org/10.6084/m9.figshare.30774995.

ACKNOWLEDGMENTS

Funding: This work was financially supported by the National Key Research and Development Program of China (2023YFA1507500 and 2022YFA1505100 to J.L.), the National Natural Science Foundation of China (BE3250011 to J.L. and 92472110 and 22173066 to T.C.), the Shanghai Municipal Science and Technology Major Project to J.L., the Natural Science Foundation of Jiangsu Province (BK20230065), the Fundamental Research Funds for the Central Universities (23X010301599 and 24X010301678 to J.L.), and the Shanghai Pilot Program for Basic Research – Shanghai Jiao Tong University (21TQ1400227 to J.L.). W.W. acknowledges support from the Photon Science Research Center for Carbon Dioxide. The authors thank beamlines BL14B1 and BL20U of the Shanghai Synchrotron Radiation Facility for providing beamtime. This work was partly supported by the Collaborative Innovation Center of Suzhou Nano Science and Technology. **Author contributions:** J.L. supervised the project. Q.Z. and J.L. conceived the idea and designed the experiments. Q.Z. and H.Li. performed all the experiments. P.L. performed the COMSOL multiphysics simulations. P.Y. carried out the DFT calculations with the supervision of T.C. N.S. contributed to figure preparation. Yi.W. and C.T. contributed to the ion chromatography testing. Y.L., Ya.W., X.Y., Zhe.L., H.S., D.L., H.Liang, and F.L. contributed to data analysis. W.W. and Y.H. conducted the synchrotron XRD measurements. L.M. assisted with the Raman experiments. J.X., Zha.L., J.M., and F.S. helped with the synchrotron XPS testing. Q.Z. and J.L. co-wrote the manuscript. All authors discussed the results and assisted with manuscript preparation. **Competing interests:** J.L., Q.Z., H.Li, and P.L. are inventors on a patent application (CN202411962196.2) related to this work filed by Shanghai Jiao Tong University. The other authors declare that they have no competing interests. **Data, code, and materials availability:** All experimental data are available in the main text or the supplementary materials. The raw numerical data, simulation data, and computational models have been deposited in Figshare (*43*).

SUPPLEMENTARY MATERIALS

science.org/doi/10.1126/science.adw5462
Materials and Methods; Figs. S1 to S67; Tables S1 to S6; References (*44*–*86*)

Submitted 11 February 2025; accepted 9 December 2025

10.1126/science.adw5462

Enhanced Li-ion diffusion improves N_2-to-NH_3 current efficiency at 100 mA cm$^{\#2}$

Qiang Zhang, Huamin Li, Peiping Yu, Pengyu Liu, Ning Sun, Yiyan Wang, Chunlai Tu, Yiping Liu, Yan Wang, Xinyang Yue, Linlin Ma, Wen Wen, Jinyang Xu, Zhaofeng Liang, Jingyuan Ma, Fei Song, Zheng Liang, Hao Sun, Daishun Ling, Hongyan Liang, Feng Liu, Yongfeng Hu, Tao Cheng, and Jun Li

Science **391** (6786), . DOI: 10.1126/science.adw5462

Editor’s summary
The Haber-Bosch process revolutionized fertilizer production a century ago and is still the predominant source of synthetic ammonia. However, it requires demanding conditions, and chemists continue to search for methods that operate closer to room temperature and pressure. One promising direction involves electrochemical reduction of dissolved lithium ions, which can in turn reduce nitrogen. Zhang *et al*. report an optimization of the solid electrolyte interphase design to enhance lithium ion flux in this process, thereby improving overall performance at current densities of 100 milliamperes per square centimeter (see the Perspective by Ampelli). —Jake S. Yeston

Science (ISSN 1095-9203) is published by the American Association for the Advancement of Science. 1200 New York Avenue NW, Washington, DC 20005. The title *Science* is a registered trademark of AAAS.